



New insight of Ag quantum dots with the improved molecular oxygen activation ability for photocatalytic applications

Jun Di ^a, Jieyang Xia ^{a,*}, Mengxia Ji ^a, Bin Wang ^a, Sheng Yin ^a, Yan Huang ^a, Zhigang Chen ^b, Huaming Li ^{a,*}

^a School of Chemistry and Chemical Engineering, Institute for Energy Research, Jiangsu University, 301 Xuefu Road, Zhenjiang 212013, PR China

^b School of the Environment, Jiangsu University, Zhenjiang 212013, PR China



ARTICLE INFO

Article history:

Received 12 December 2015
Received in revised form 24 January 2016
Accepted 26 January 2016
Available online 29 January 2016

Keywords:

Ag
BiOBr
Molecular oxygen activation
Hot electron
Photocatalytic

ABSTRACT

Ag quantum dots (Ag QDs) modified BiOBr ultrathin nanosheets have been prepared via the reactable ionic liquid assisted solvothermal method. The Ag QDs were evenly dispersed on the surface of BiOBr nanosheets with the diameter less than 5 nm. The obtained Ag QDs/BiOBr materials displayed greatly enhanced photocatalytic activity for the degradation of antibiotic agent ciprofloxacin (CIP) and tetracycline hydrochloride (TC) under visible light irradiation. Through the various characterizations, the relationship between structure and activity was studied in details and some new insights of the key role of Ag QDs for the enhanced photocatalytic activity was presented. Different from the roles previous reported such as electron injection, plasmon resonance energy transfer and Schottky junction, the modified Ag QDs could active the molecular oxygen via the hot electron reduction under the visible light irradiation in this system. And the Ag QDs worked as adsorption centers, charge separation centers and photocatalytic reaction centers, contributed to the increased photocatalytic activity. This study provided an approach to improve the molecular oxygen activation for pollutant removal, selective organic synthesis or donating abundant hot electrons for CO₂ photoreduction.

© 2016 Elsevier B.V. All rights reserved.

1. Introduction

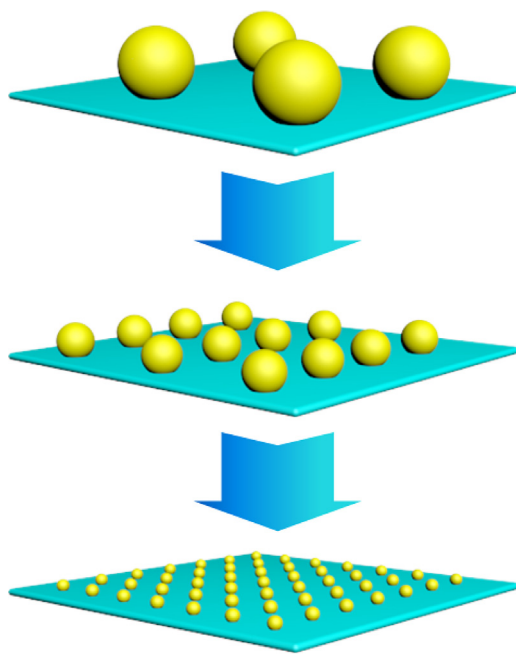
Semiconductor photocatalysis has emerged as a green, sustainable technology to addressing the increasingly energy shortage and environmental pollution issues [1,2]. Numerous attempts have been carried out to achieve excellent photocatalysts for water purification, water splitting, nitrogen fixation, CO₂ reduction for solar fuels production and so on [3–8].

Metal nanoparticles (such as Pt, Pd, Au, Cu, Bi, Ag) modified semiconductor photocatalysts has been widely studied for maximizing the performance of photocatalytic reactions due to the metal nanoparticles can work as capture center for photogenerated charge carriers, facilitating effective separation of electron-hole pairs [9]. In recent years, plasmonic photocatalysts have become the focus in photocatalysis field since the Awazu et al. found the surface plasmon resonance (SPR) effect of Ag nanoparticles could improve the photocatalytic activity for pollutant degradation [10]. Different from the function of capture center, the SPR of metal

nanoparticles such as Ag, Au, Bi was believed to be responsible for the increased photocatalytic activity [11,12]. The SPR was produced by the plasmonic metal NPs created a coherent oscillation of the free electrons in resonance with the electrical field of the incoming electromagnetic irradiation. Take Ag NPs for instance since it always exhibited the better SPR effects than other noble metals. Following the light absorption and SPR excitation in metal nanoparticles, the plasmon decay could take place through three mechanisms [13], (1) elastic radiative reemission of photons, (2) nonradiative Landau damping, where the photon energy was converted to single e[−]/h⁺ pair excitations; the excited primary electrons interact with other electrons through Coulombic inelastic scattering to produce many electrons, and (3) the interaction of excited surface plasmons with adsorbates, inducing a direct electron injection into the adsorbates. Up to now, several systems such as Ag/TiO₂ [14], Ag/AgCl [15], Ag/Cu₂O [16], Ag/BiOX (X = Cl, Br, I) [9,17,18], Ag/g-C₃N₄ [19], Ag/Bi₂WO₆ [20], and Ag/AgX/BiOX (X = Cl, Br) [21,22] have been reported. The results suggested that the Ag modification could improve the photocatalytic activity of the body photocatalyst. However, the mechanism of activity improvement in different systems above mentioned was conflict. For example, Zhu's group considered that the Ag nanoparticles mainly acted as the reservoir

* Corresponding authors.

E-mail addresses: xjx@ujs.edu.cn (J. Xia), lhlm@ujs.edu.cn (H. Li).



Scheme 1. Design plans of Ag QDs modified BiOBr ultrathin nanosheets.

of photoelectrons generated from C_3N_4 to increase the separation efficiency of electron-hole pairs [19]. Jiang's group regard as the Ag nanoparticles would produce the near-field electromagnetic radiative energy to boost the generation of charge carriers within TiO_2 nanotube and thus result in excellent photocatalytic performance [14]. Zhang's group demonstrated the Ag nanoparticles would produce SPR-excited electrons under visible light irradiation and then efficiently inject to the conduction band of BiOCl to improve the photocatalytic activity [17]. Therefore, the substance of metal NPs for the enhanced photocatalytic activity should be further explored in details.

Recently, BiOX ($\text{X}=\text{Cl}, \text{Br}, \text{I}$) have been widely studied due to its high-efficiency photocatalytic activity under visible or UV light irradiation [23–29]. The unique layered structure of BiOX by interleaved $[\text{Bi}_2\text{O}_2]$ slabs with double slabs of halogen atoms could result in the inherent internal static electric fields [30]. It could lead to the effective separation of electron-hole pairs and the electrons would migrate to and accumulate in the (001) facet along with the holes migrate to (110) facet [18]. Among these BiOX materials, BiOBr was of great research interest since its suitable energy band structure and high-efficiency visible-light response photocatalytic activity [31–33]. Up to now, several strategies have been employed to construct the BiOBr -based materials for optimizing the photocatalytic performance, such as tailored crystal facets [34,35], element doping or defect controlling [36], dehalogenation [37,38], and heterologous hybridization [39–46]. However, it was still far from enough for potential applications and need to further increased the photocatalytic activity. Considering the materials with ultrathin structure could enable more exposed surfaces so as endowing more surface active sites, the BiOBr with ultrathin thickness may be the desired architecture. At the same time, compared to the bulk materials, the BiOBr with ultrathin structure could enable the strikingly fast carrier transport from the inside to the surface, thus the higher separation efficiency of charge carriers can be achieved and advanced photocatalytic activity can be obtained [47]. What's more, consider the advantages of Ag NPs, it motive us to construct the Ag NPs modified BiOBr ultrathin nanosheets to obtain the superior photocatalytic performance. Due to the large size Ag NPs could not display sufficient and favorable interface contact with BiOBr (Scheme 1),

we try to reduce the size of Ag NPs to less than 5 nm (Ag quantum dots (Ag QDs)), which could lead to the highly dispersion of Ag NPs. Since the small size of Ag QDs, the interface mismatch between the BiOBr ultrathin nanosheets and Ag QDs can be minimized, and the nanoscale heterojunctions with intimate interface contacts can be constructed.

In this study, Ag QDs modified BiOBr ultrathin nanosheets have been prepared through a facile ionic liquid assisted solvothermal method. The structures, morphologies, optical and electronic properties of the obtained materials was investigated. The photocatalytic performance was evaluated by the degradation of antibiotic agent ciprofloxacin (CIP), tetracycline hydrochloride (TC) and rhodamine B (RhB) under visible light irradiation. The structure-activity relationships and photocatalytic mechanism were discussed in details along with some new insight regarding the mode of action of Ag QDs for the improved photocatalytic activity was provided.

2. Experimental

2.1. Material and sample preparation

Phenol rhodamine B (RhB), antibacterial agent ciprofloxacin (CIP) and tetracycline hydrochloride (TC) were purchased from Sinopharm and used without further treatment. The ionic liquid 1-hexadecyl-3-methylimidazolium bromide ($[\text{C}_{16}\text{mim}]\text{Br}$) (99%) was obtained from Shanghai Chengjie Chemical Co. Ltd.

Ag quantum dots (Ag QDs) was prepared according to the reported literature [48]. 0.38 g AgNO_3 was added into 20 mL of oleylamine (OAm) and 0.4 mL of oleic acid (OA), and the magnetically stirred mixture was heated to 120 °C for 18 h. After cooled down to room temperature, 30 mL acetone was added to precipitate the product. After washing with ethanol for several times, the obtained Ag QDs was redispersed in 20 mL hexane.

In a typical synthesis of Ag QDs/ BiOBr -0.5 materials, 1 mmol $[\text{C}_{16}\text{mim}]\text{Br}$ and 0.5 mL of Ag QDs hexane solution were dispersed into 8 mL ethanol to obtain solution A. 1 mmol $\text{Bi}(\text{NO}_3)_3 \cdot 5\text{H}_2\text{O}$ was dissolved into 8 mL ethylene glycol (EG) to obtain solution B. The solution A was added into solution B dropwise under stirring and further stirred for 30 min. Then suspension was sealed in a 25 mL teflon-lined stainless-steel autoclave and heated at 140 °C for 24 h. The product was collected after centrifugation, washed with deionized water and ethanol for several times, and dried at 50 °C. Pure BiOBr and Ag QDs/ BiOBr samples with different content of Ag QDs were synthesized using a similar route by tuning the addition of Ag QDs (0, 0.3, 0.5 and 1 mL).

Ag particles were prepared via the EG assisted solvothermal process. 0.1 g AgNO_3 was added into 20 mL EG and solvothermal treatment at 140 °C for 24 h. And the 0.5 wt% Ag/ BiOBr and 1 wt% Ag/ BiOBr materials were prepared using the above mentioned method only by using Ag particles for replacing the Ag QDs.

2.2. Characterization

The powder X-ray diffraction (XRD) were recorded on a Shimadzu XRD-6000 X-ray diffractometer with monochromatized $\text{Cu K}\alpha$ radiation ($\lambda = 0.15418 \text{ nm}$). The XPS spectra were collected by an ESCALab MKII X-ray photo-electron spectrometer and all binding energies were calibrated by using the contaminant carbon (C1s = 284.6 eV) as a reference. A micro Raman spectrometer (Renishaw Invia) was employed to collect the Raman spectra in a backscattering geometry with a 532 nm laser as an excitation source. The morphology of the prepared Ag QDs/ BiOBr were analyzed through a scanning electron microscope (SEM) (JSM-7001F, JEOL) equipped with an energy-dispersive X-ray spec-

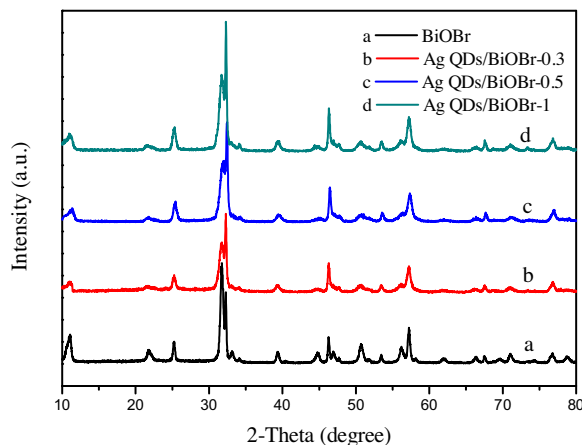


Fig 1. XRD spectra of the obtained pure BiOBr and Ag QDs/BiOBr materials with different Ag QDs contents.

troscope (EDS) and a transmission electron microscopy (TEM) (JEOL JSM-2100). Diffuse reflection spectra (DRS) were obtained on a UV-2450 UV-vis spectrophotometer and BaSO₄ was employed as the reflectance standard in the experiment. The Brunauer-Emmett-Teller (BET) surface area was measured by a TriStar II 3020 Surface Area and Porosity Analyzer with the nitrogen as absorbed gas. The photoluminescence (PL) intensity of the prepared samples was characterized using a Varian Cary Eclipse spectrometer. The electron spin resonance (ESR) signals of spin-trapped radicals were conducted on a Bruker model ESR JES-FA200 spectrometer using spin-trap reagent DMPO (Sigma Chemical Co.) in water and methanol, respectively.

2.3. Photocatalytic activity measurement

The photocatalytic activity of the obtained Ag QDs/BiOBr materials were evaluated by the degradation of antibiotic agent ciprofloxacin (CIP), tetracycline hydrochloride (TC), and rhodamine B (RhB) under visible light irradiation. 50 mg, 50 mg and 20 mg photocatalysts was added to 100 mL model pollutant solution of CIP (10 mg L⁻¹), TC (20 mg L⁻¹) and RhB (10 mg L⁻¹), respectively, and

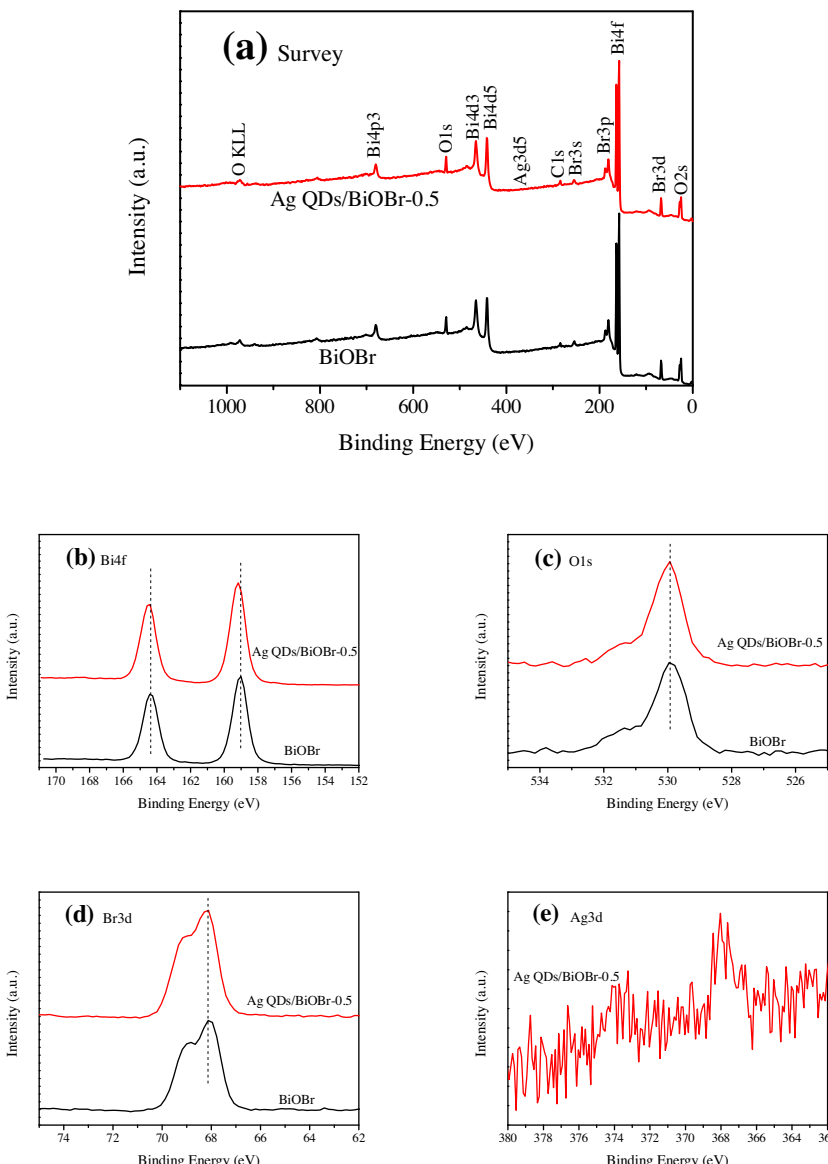


Fig. 2. X-ray photoelectron spectra: (a) full scan, (b) Bi 4f, (c) O 1s, (d) Br 3d, and (e) Ag 3d regions of Ag QDs/BiOBr materials.

stirred for 30 min in the dark to achieve the absorption-desorption equilibrium. The light source was a 300 W Xe arc lamp with a 400 nm cutoff filter. The distance between the light source and the model pollutant was 10 cm. Aeration was carried out using an air pump to ensure a constant supply of oxygen and full mixing of the solution and the photocatalysts. At given time intervals, 3 mL suspension were sampled and centrifuged to remove the photocatalyst particles. The concentrations of CIP, TC and RhB at different conditions were analyzed by recording variations of the maximum absorption peak at 276 nm, 356 nm and 553 nm, respectively, using the UV-vis spectra (UV-2450, Shimadzu).

2.4. Electrochemical measurements

All electrochemical tests were performed in a conventional three-electrode cell with a Pt wire as the counter electrode, and an Ag/AgCl/sat. KCl electrode as the reference electrode. The sample was deposited as a film formed on an indium-tin-oxide (ITO) conductive glass with the fixed area of 0.5 cm². The photocurrent and electrochemical impedance spectroscopy (EIS) measurement were performed on a CHI 660B electrochemical system (Chenhua Instruments). The photocurrent was performed in phosphate buffer solution (PBS, 0.1 M, pH 7.0) with a 500 W Xe lamp as light source. The EIS measurement was carried out in the 0.1 M KCl solution containing 5 mM $\text{Fe}(\text{CN})_6^{3-}/\text{Fe}(\text{CN})_6^{4-}$.

3. Results and discussion

3.1. Compositional and structural information

The crystal structure and phase composition of the as-prepared BiOBr and Ag QDs/BiOBr materials were characterized by X-ray diffraction (XRD) analysis (Fig. 1). All the diffraction peaks can be indexed to tetragonal phase of BiOBr (JCPDS card No. 73-2061) with the lattice parameters of $a=0.3915$ nm and $c=0.8076$ nm. No peak shift was found when Ag QDs was introduced into the BiOBr, revealing that the formation of the hybrid materials with the present content of Ag has a negligible effect on the crystal phase of BiOBr materials. However, no typical diffraction peaks of Ag can be observed in the Ag QDs/BiOBr materials, which can be explained as the low amount of Ag QDs and the low crystallinity of minisize Ag QDs.

The surface atomic composition and the chemical state of the Ag QDs/BiOBr materials were investigated by using X-ray photoelectron spectroscopy (XPS). As depicted in Fig. 2a, the Ag QDs/BiOBr sample was consisted of five elements, Bi, O, Br, Ag and adventitious carbon. From the high-resolution XPS spectra of Bi elemental in Fig. 2b, it can be clearly recognized that the binding energy of 159.0 and 164.3 eV was corresponding to the Bi 4f7/2 and Bi 4f5/2, respectively, in good agreement with that of Bi^{3+} . In comparison with BiOBr, the Bi 4f peak in Ag QDs/BiOBr-0.5 material shifted to the higher binding energy, indicating the existence of interactions between the modified Ag QDs and BiOBr materials [49]. From Fig. 2c and 2d, the peaks centered at 529.9 and 68.1 eV can be attributed to the O 1s and Br 3d, respectively. In the high-resolution XPS spectra of Ag element in Ag QDs/BiOBr-0.5 material (Fig. 2e), two peaks at binding energies of 368.0 and 374.1 eV can be observed and can be ascribed to the of Ag 3d5/2 and Ag 3d3/2 of metallic Ag, respectively [17].

Raman spectra have been employed to further explore the surface microstructures of Ag QDs/BiOBr, as shown in Fig. 3. Three Raman bands located at 56.8, 113.2, and 159.9 cm⁻¹ can be seen for pure BiOBr, which can be attributed to the external A_{1g} , internal A_{1g} , and E_{1g} internal Bi-Br stretching modes, respectively [50,51]. Raman spectra of Ag QDs/BiOBr exhibited several distinct changes

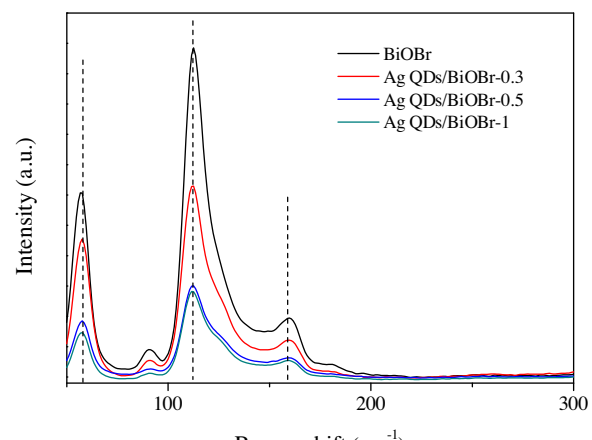


Fig. 3. Raman spectra of BiOBr and Ag QDs/BiOBr materials.

including the peak intensity decrease and the shift of vibration peak. Three features were evident: (1) the peak intensity gradually decreased with the increase of Ag QDs content, indicating the crystallinity weakening by Ag QDs introduction, (2) shifting of the E_{1g} mode at 159.9 cm⁻¹ to lower frequency, (3) the blue shift of external A_{1g} from 56.8 cm⁻¹ for BiOBr to 58.0 cm⁻¹ for Ag QDs/BiOBr-1 sample. This indicated that the surface chemical environment in the Ag QDs/BiOBr has changed and can be referred to the presence of interaction between Ag QDs and BiOBr in the Ag QDs/BiOBr sample.

3.2. Morphology and textural property

The morphologies of BiOBr and Ag QDs/BiOBr samples were characterized by field-emission scanning electron microscopy (FESEM). The pure BiOBr appeared of nanosheets structure with the size about 300*300 nm (Fig. 4a, b). With respect to the Ag QDs/BiOBr-0.5 sample (Fig. 4c, d), the nanosheets structure can also be found and the thickness of nanosheets can be determined to be 10 nm viewing from the vertical nanosheets, revealing the ultra-thin structure of BiOBr nanosheets. The microstructure of the Ag QDs/BiOBr material was further investigated by transmission electron microscopy (TEM). As shown in Fig. 5a, the as-prepared Ag nanoparticles displayed the size less than 5 nm, indicating the successful preparation of Ag QDs. The TEM image of Ag QDs/BiOBr-0.5 was displayed in Fig. 5b, c. A lot of dark dots were distributed on the relatively bright nanosheets, implying that Ag QDs have been deposited on the surface of BiOBr nanosheets (Fig. 5b). The formation of Ag QDs/BiOBr hybrid nanosheets was further proved by HRTEM analysis (Fig. 5c). It can be seen that the Ag QDs and BiOBr have distinct lattice spacing. The lattice spacing of 0.224 nm corresponded to the (1-12) crystal plane of Ag (JCPDS 41-1402). The observed lattice fringe of the BiOBr crystallite was determined to be 0.277 nm, which corresponded to the (110) crystal plane of BiOBr (JCPDS 73-2061). The EDS analysis (Fig. 5d) displayed that the Ag QDs/BiOBr-0.5 sample composed of Ag, Bi, O, and Br elements, with the content of Ag was about 0.53 wt%. Based on the elemental mapping images, it can be seen that the Ag, Bi, O, and Br elements were uniform distributed in the Ag QDs/BiOBr materials (Fig. 6). The above results strongly revealed that the Ag QDs have been successfully loaded on the surface of BiOBr nanosheets with the evenly distribution of Ag QDs.

The N_2 adsorption-desorption isotherms were employed to investigate the surface area and pore structure of these samples (Fig. 7). The isotherms for the BiOBr and Ag QDs/BiOBr ultrathin nanosheets were of type IV, which was typically associated with capillary condensation in mesopores. The mesopores were origi-

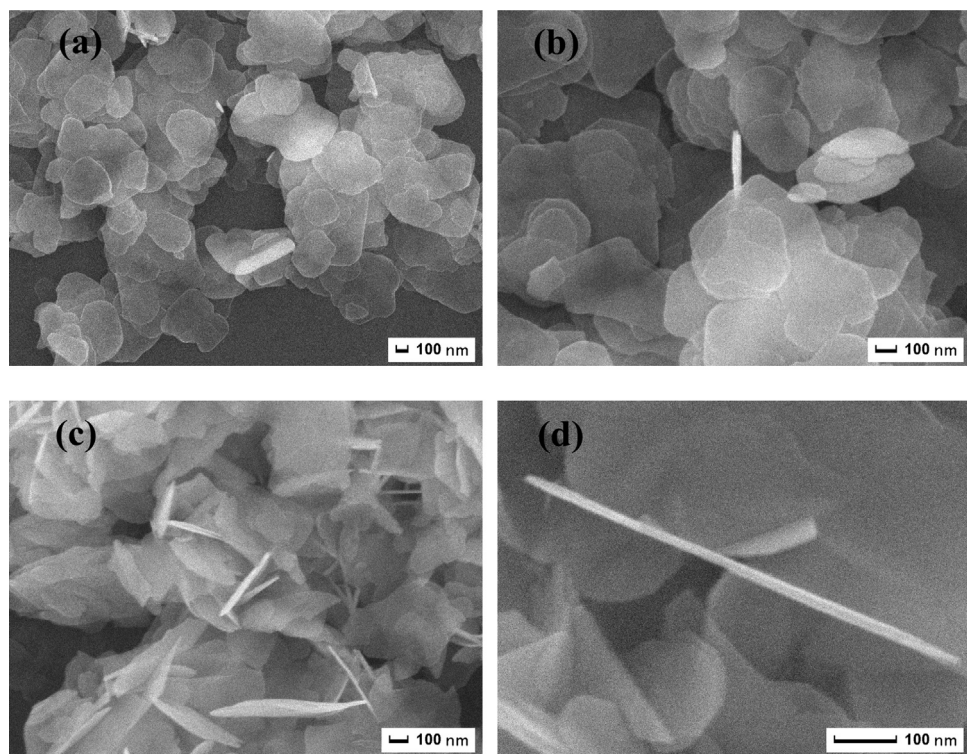


Fig. 4. SEM images of (a, b) pure BiOBr and (c, d) Ag QDs/BiOBr-0.5 materials.

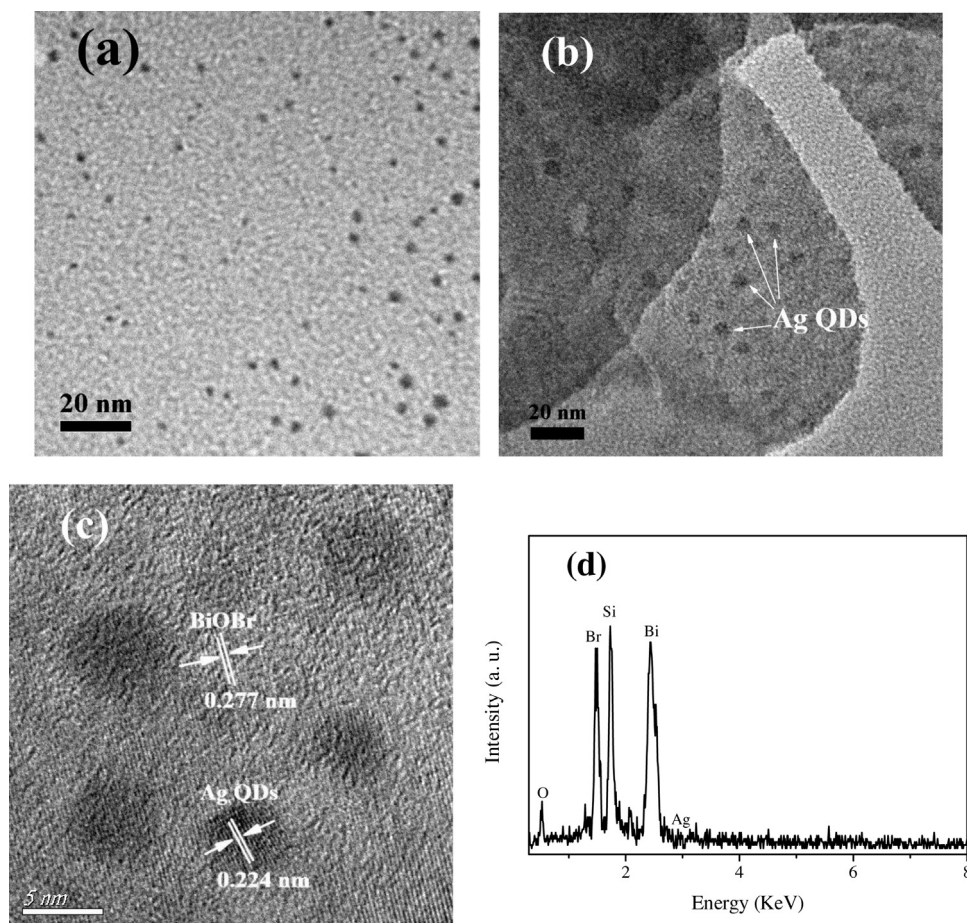


Fig. 5. TEM images of (a) Ag QDs, (b) Ag QDs/BiOBr-0.5 material; (c) HRTEM image of Ag QDs/BiOBr-0.5 sample; (d) EDS of the Ag QDs/BiOBr-0.5 material.

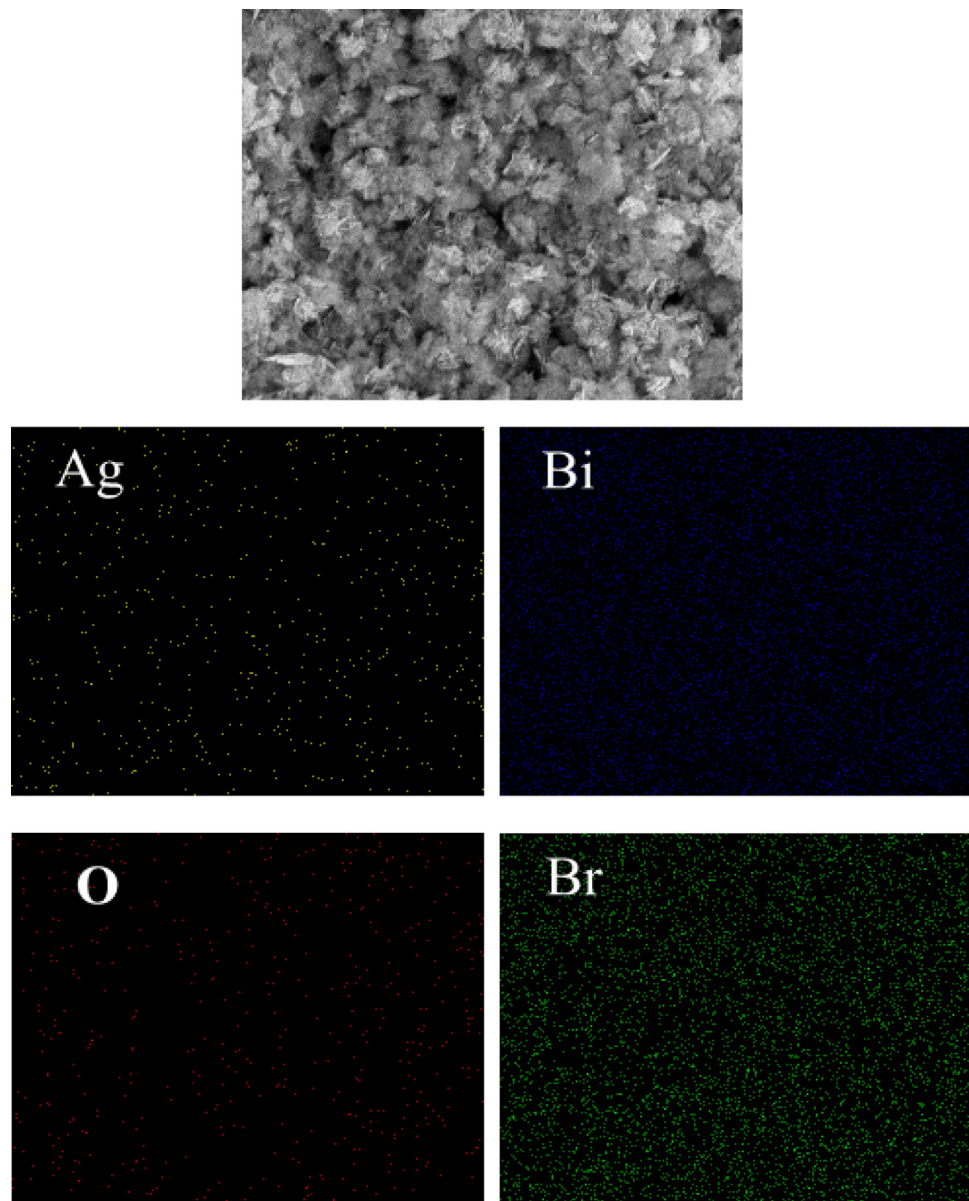


Fig. 6. Typical SEM image of Ag QDs/BiOBr-0.5 materials and corresponding elemental mapping images of Ag, Bi, O, and Br.

nated from the inter-nanosheet spacing [52]. In this system, the BET surface area values of the Ag QDs/BiOBr materials enhanced with the increased Ag QDs content (10.50, 14.28, 16.93 and 19.13 m²/g for the pure BiOBr, Ag QDs/BiOBr-0.3, Ag QDs/BiOBr-0.5 and Ag QDs/BiOBr-1, respectively). From the pore size distribution curves, it can be found that the introduction of Ag QDs did not obviously affect the pore size and pore volume. Therefore, the improved surface area may not derive from the pore size and pore volume while it may result from the ultrasmall size of Ag QDs structure. The high fraction coordination-unsaturated surface atoms that comparable to the overall atoms of Ag QDs could act as the adsorption sites and further increased the specific surface area [53]. Thus, the Ag QDs in this system would work as adsorption centers which was beneficial to adsorb more pollutants and active species on the surface during the photocatalysis process, and then resulted in the increased photocatalytic activity.

3.3. Optical absorption properties

The optical properties of the Ag QDs/BiOBr samples were analyzed via the UV-vis diffuse reflectance spectra (DRS) measurement (Fig. 8). Only an absorption band with the onset absorption edge about 430 nm can be observed for BiOBr nanosheets, which can be ascribed to the band-to-band transition. After the Ag QDs was introduced, the absorption band edge of the Ag QDs/BiOBr ultrathin nanosheets did not exhibited distinct variation when compared to the BiOBr nanosheets, suggesting the band structure of BiOBr has not been affected. However, the light harvesting capability within the 430 nm to 800 nm gradually improved with the higher Ag QDs contents [54]. The light harvesting ability of semiconductors could significantly influence their photocatalytic activity. Thus, the enhanced light harvesting capability which stem from the Ag QDs modification may bring about increased photocatalytic activity. The band gap energy of the pure BiOBr materials was determined to be 2.79 eV by the calculation via the classical Tauc approach (Fig. 8b).

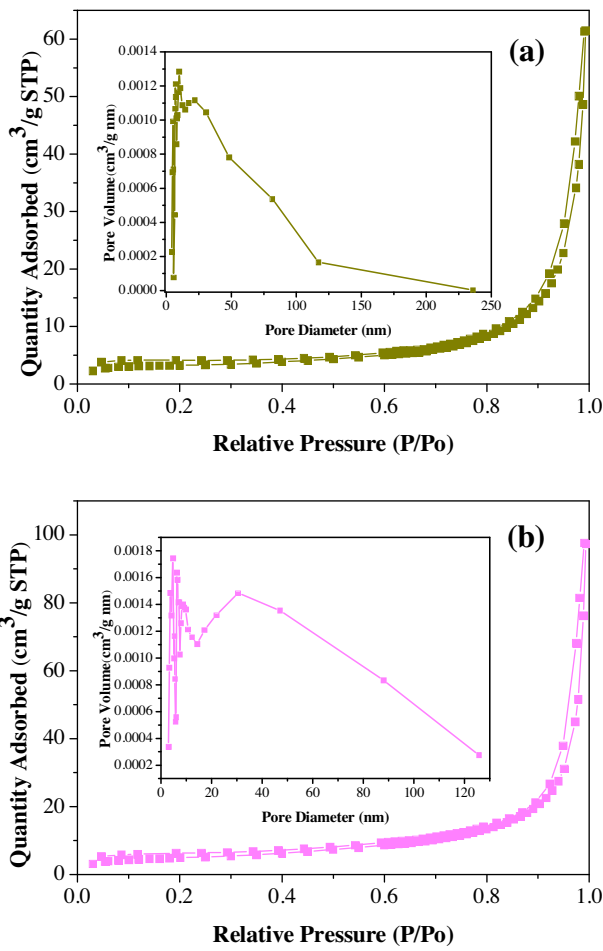


Fig. 7. Nitrogen adsorption-desorption isotherms and the corresponding pore-size distribution curves (inset) of the (a) BiOBr, (b) Ag QDs/BiOBr-0.5 materials.

3.4. Photocatalytic tests

The photocatalytic performance of the BiOBr and Ag QDs/BiOBr materials was evaluated by the photocatalytic degradation of RhB, CIP and TC aqueous solution, as shown in Fig. 9. As one of the most commonly model pollutants, RhB has been first employed to evaluate the photocatalytic activity of Ag QDs/BiOBr materials (Fig. 9a). Only 32.3% of RhB can be degraded by pure BiOBr after the irradiation of visible light for 10 min. After the Ag QDs was modified on the BiOBr, the photocatalytic activity greatly improved and the Ag QDs/BiOBr-0.5 sample displayed the highest activity. 83.8% of RhB can be removed by Ag QDs/BiOBr-0.5 after 10 min and the degradation efficiency can reach 97.9% after 20 min. Consider the low content of Ag (0.53 wt%) in the Ag QDs/BiOBr-0.5, the greatly enhanced activity was attributed to the ultrasmall size of Ag QDs which construct evenly distribution and tight combination with BiOBr and thus enable the sufficient utilization of Ag. In order to make a comparison, the 0.5 wt% Ag/BiOBr and 1 wt% Ag/BiOBr sample with the large size of Ag were also employed for the degradation of RhB. The XRD analysis (Fig. S1) indicated the 0.5 wt% Ag/BiOBr and 1 wt% Ag/BiOBr samples have been prepared successfully. As shown in Fig. S2, only bits of improvement can be obtained for 0.5 wt% Ag/BiOBr and 1 wt% Ag/BiOBr samples, suggesting the construction of ultrasmall Ag QDs on the ultrathin BiOBr nanosheets was an effective approach to achieve the sufficient utilization of Ag and obtain the high-efficiency photocatalyst. It was worth noting that the obtained Ag QDs/BiOBr materials in this system displayed higher photocatalytic activity than the mostly

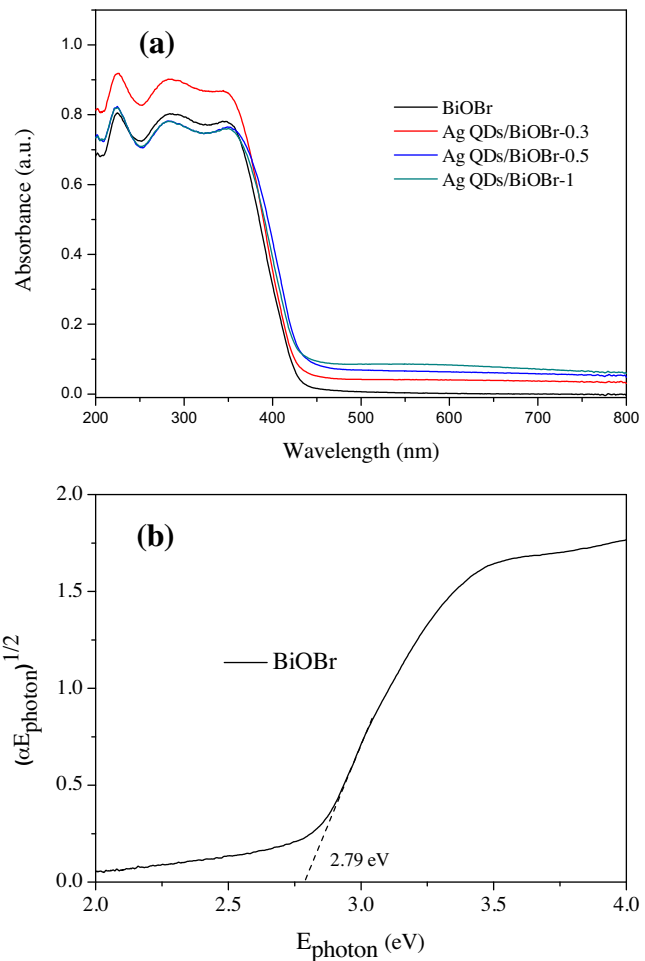


Fig. 8. (a) UV/Vis diffuse reflection spectra of pure BiOBr and Ag QDs/BiOBr materials; (b) Tauc plot of the pure BiOBr.

reported BiOBr-based materials [26,35,36,39,42–44,51,55,56]. To test the stability of the Ag QDs modified BiOBr nanosheets, the Ag QDs/BiOBr-0.5 material was collected after the photodegradation of RhB under the irradiation of visible light. As shown in Fig. S3, the photocatalytic activity could still be maintained after four cycles with only 3.3% decrease of the degradation efficiency. This result indicated that the Ag QDs/BiOBr material may be the candidate for the potential applications.

The photocatalytic activity of Ag QDs/BiOBr materials was further evaluated by the degradation of colorless CIP and TC under visible light irradiation. Antibiotic agents have been widely employed for treating bacterial infections. However, the vast discharge of antibiotic agents to natural environments would generate several human health concerns since it could induce the proliferation of bacterial drug resistance. As typical antibiotic agents, it was of significance to study the removal of CIP and TC. As shown in Fig. 9b, 45.9% of CIP can be degraded by BiOBr under visible light irradiation for 180 min. When the Ag QDs was modified on the BiOBr, the photocatalytic activity was improved. The law of the enhanced activity was consistent to the RhB degradation along with the Ag QDs/BiOBr-0.5 showed the highest activity and 79.3% CIP can be removed within the same time. Similarly, the introduction of Ag QDs could also improve the photocatalytic activity for the degradation of TC under visible light irradiation. As shown in Fig. 9c, only 33.1% of TC was degraded over pure BiOBr for 120 min irradiation. However, the Ag QDs modification could improve the photocatalytic activity significantly. After 120 min irradiation,

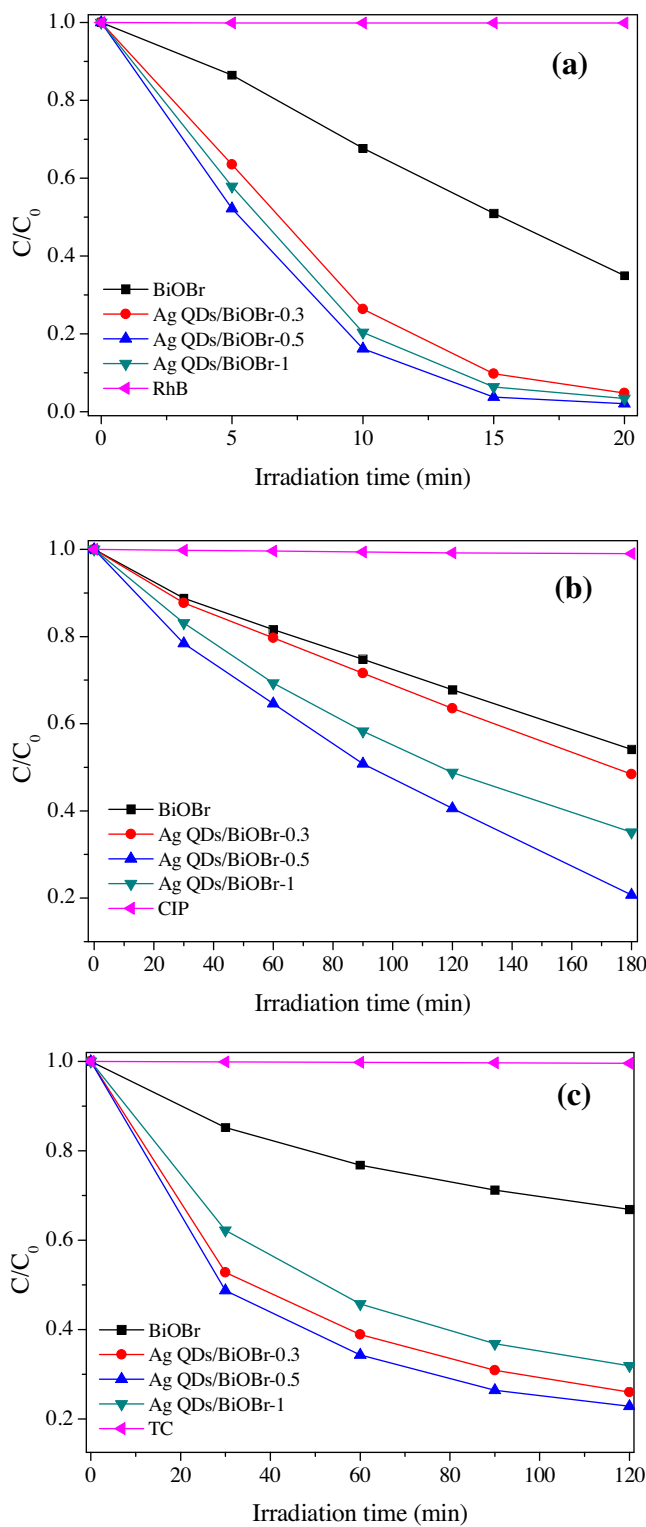


Fig. 9. Photocatalytic degradation of (a) RhB, (b) CIP and (c) TC over BiOBr and Ag QDs/BiOBr materials under visible light irradiation.

74.0%, 77.2% and 68.1% of TC can be degraded by Ag QDs/BiOBr-0.3, Ag QDs/BiOBr-0.5 and Ag QDs/BiOBr-1 sample, respectively. The Ag QDs/BiOBr-0.5 material exhibited the highest photocatalytic performance. Based on the photodegradation results, it was reasonable to suggest that Ag QDs modification could greatly increase the photocatalytic activity and the Ag QDs/BiOBr material was efficient visible-light-driven photocatalyst.

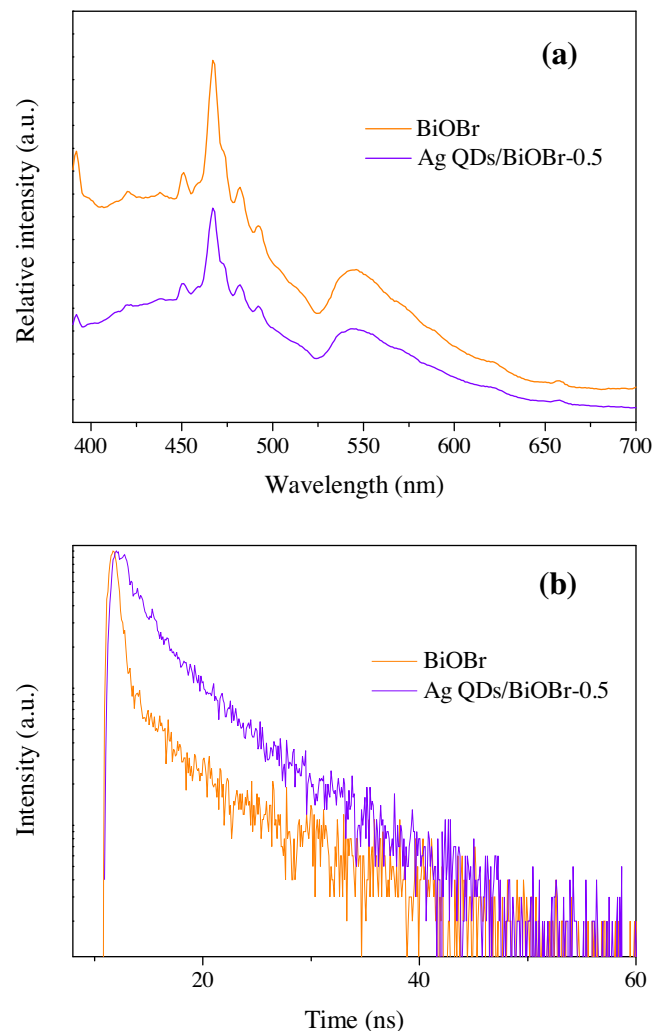


Fig. 10. (a) Steady-state PL spectra and (b) time-resolved transient PL decay for the prepared BiOBr and Ag QDs/BiOBr-0.5 materials.

3.5. Structure-activity relationships and mechanism insight

Photoluminescence (PL) spectroscopy was useful for revealing the transfer and separation efficiency of photogenerated electron-hole pairs. In this case, the charge separation and transfer ability of the obtained BiOBr and Ag QDs/BiOBr sample was first studied by steady-state PL analysis and the result was shown in Fig. 10a. The BiOBr sample displayed the emission peak centered at around 465 nm under the excitation wavelength of 360 nm. After the Ag QDs was introduced to the BiOBr, the PL intensity become much lower, suggesting the Ag QDs modification could enable the effective separation of photo-generated charge carriers [57]. Normally, the Ag nanoparticles could generate the electron-hole pairs due to the surface plasmon resonance effect and the electron would inject into the conduction band (CB) of BiOBr. However, in this way, the PL intensity of Ag QDs/BiOBr would not decrease due to the recombination of photo-generated charge carriers could not be effectively inhibited. And if the Ag QDs induced near-field electromagnetic radiative energy to boost the generation of more charge carriers within semiconductors, the PL intensity of Ag QDs/BiOBr would be stronger. Therefore, the Schottky junction on the BiOBr (001) facet may offer a stronger driving force for electron trapping. The previous report has demonstrated the electron photo-generated within the BiOBr would accumulate on (001) facet and hole on (110) facet due to the built-in field [18]. Due to the BiOBr in this system was

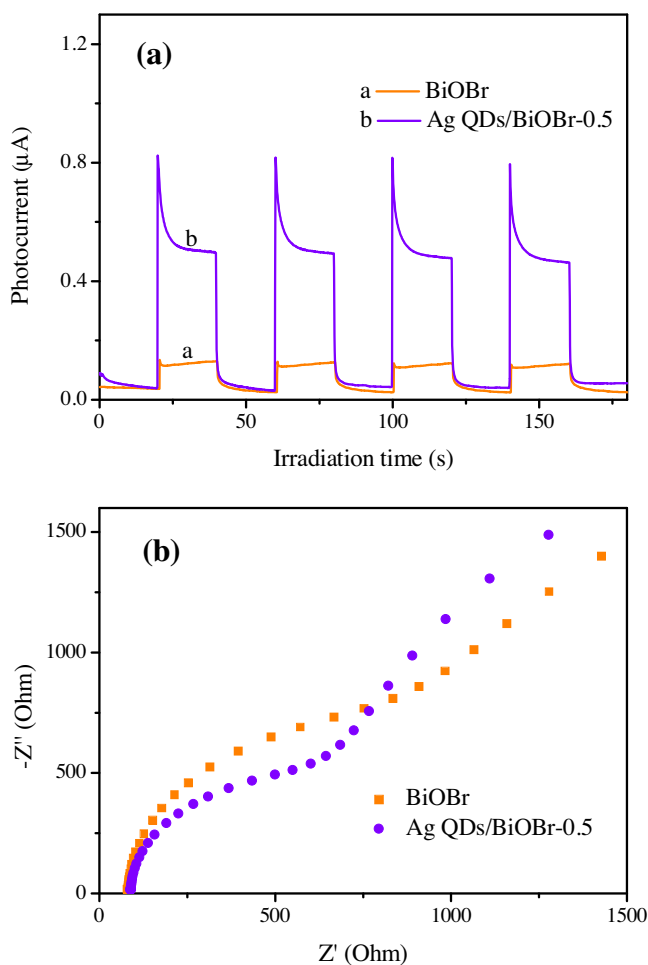


Fig. 11. (a) Transient photocurrent responses under visible light irradiation, (b) electrochemical impedance spectroscopy (EIS) Nynquist plots of pure BiOBr and Ag QDs/BiOBr-0.5 electrodes.

exposed with (001) facet and Ag QDs was modified on (001) facet of BiOBr, the accumulated electrons in the CB of BiOBr could flow into metal Ag QDs through the Schottky barrier since the CB potential of BiOBr was more negative than the Fermi level of the Ag QDs. Thus, the effective separation of photo-generated charge carriers in BiOBr could be obtained. From the time-resolved transient PL spectra (Fig. 10b), it can be found that the lifetime of charge carriers in Ag QDs/BiOBr-0.5 sample was much longer than pure BiOBr, suggesting the higher separation efficiency of photo-generated charge carriers for the Ag QDs/BiOBr can be achieved.

For better understanding, the effective separation of photo-generated charge carriers in the Ag QDs/BiOBr materials can be further proved by photocurrent analysis. From Fig. 11a, it can be found that Ag QDs/BiOBr materials exhibited improved photocurrent response compared with pure BiOBr owing to the increased photogenerated charge carrier separation performance at the interface. This result indicated that the modification of Ag QDs could be benefit to the efficient utilization of the solar-light resource [58]. The results above mentioned can be further supported by electrochemical impedance spectra (EIS) analysis. It can be seen from Fig. 11b that Ag QDs/BiOBr sample displayed the smaller impedance arc radius than that of BiOBr, manifesting the better electrical conductivity, which would facilitate the transfer of electrons and thus boost the photocatalytic efficiency [59].

The electron spin resonance (ESR) spectra was carried out for BiOBr and Ag QDs/BiOBr materials to determine the main active

species during the photocatalysis process [60]. When the light was on, four weak characteristic peaks of the DMPO-superoxide radical ($O_2^{\cdot-}$) could be observed for pure BiOBr sample (Fig. 12a). It implied that only bits of $O_2^{\cdot-}$ can be generated under the visible light irradiation. However, no characteristic signals of DMPO-hydroxyl radical ($\cdot OH$) can be found, suggesting the $\cdot OH$ may not be the main reactive species (Fig. 12b). After the Ag QDs was modified on the BiOBr, the intensity of DMPO- $O_2^{\cdot-}$ signals greatly increased (Fig. 12c). Due to the $O_2^{\cdot-}$ was generated via one-electron reduction of O_2 , the higher $O_2^{\cdot-}$ intensity of Ag QDs/BiOBr materials indicating the enhanced molecular oxygen activation ability can be obtained by the introduction of Ag QDs. Similar to the BiOBr, $\cdot OH$ was also not the main active species for Ag QDs/BiOBr sample (Fig. 12d). Free radicals trapping experiments were further carried out to reveal the main active species during the photocatalysis process (Fig. 13). The addition of *p*-benzoquinone (BQ) and disodium ethylenediaminetetraacetate (EDTA-2Na) could greatly suppress the photocatalytic activity for the degradation of RhB, suggesting the $O_2^{\cdot-}$ and holes played important role for the photodegradation process [61]. When the isopropyl alcohol (IPA) was added, no obviously affection of degradation efficiency can be seen, implying the $\cdot OH$ was not the main active species. The results of free radicals trapping experiment were agree with the ESR analysis.

To gain further insight into the intrinsic reasons that the introduction of Ag QDs to BiOBr can increase the molecular oxygen activation ability under the visible light irradiation, the XPS valence spectra were performed. The valence band (VB) of BiOBr primarily resulted from the hybridization of the O 2p and Br 4p orbitals, and the Bi 6p states contributed to the conduction band (CB). As shown in Fig. 14, the VB value of the BiOBr was determined to be 1.88 eV. After the Ag QDs was introduced, the total density of states of electronic states above the VB of BiOBr was no changed, revealing the energy band structure variation was not the origin of the increased molecular oxygen activation ability. According to the formula $E_{CB} = E_{VB} - E_g$ and the E_g value obtained from DRS was 2.79 eV, the CB minimum will occur at about -0.91 eV. Thus, the photogenerated electrons on the CB of BiOBr could reduce the O_2 to $O_2^{\cdot-}$ and the holes on the VB could not oxidize the OH^- to produce the $\cdot OH$, owing to the $E^\circ(O_2/O_2^{\cdot-})$ was about -0.046 eV and the $E^\circ(OH/OH^-)$ was 2.38 eV vs. NHE [62]. However, the electron generated by the BiOBr was not energetic and the low separation efficiency of electron-hole pairs limited the molecular oxygen activation process. When the Ag QDs was modified on the BiOBr, the accumulated electrons in the CB of BiOBr could flow into Ag QDs. However, the Fermi level of Ag was 0.4 V (vs. NHE) [63,64], which was not able to reduce O_2 to generate $O_2^{\cdot-}$. Therefore, if Ag QDs only acted as the electrons collector, there would not be greatly enhanced $O_2^{\cdot-}$ in the Ag QDs/BiOBr. It seemed some inconsistent with the results of PL and photocurrent which indicated the Ag QDs work as the Schottky junction. Based on the above results, it can be reasonable to suggest some new insight that the holes could generate in the Ag QDs via the surface plasmon resonance effect and then it could combine with the electrons from the BiOBr, leaving the energetic photogenerated hot electrons in the excited state Ag QDs. The hot electrons in the Ag QDs were energetic robustly to active molecular oxygen via the one-electron reduction. This result was in accordance with the ESR analysis.

According to the BET analysis, the introduction of Ag QDs would improve the surface area of Ag QDs/BiOBr samples and the Ag QDs could act as the adsorption centers to adsorb pollutants on its surface. However, the BET surface area of Ag QDs/BiOBr-0.3, Ag QDs/BiOBr-0.5 and Ag QDs/BiOBr-1 samples were 14.28, 16.93 and 19.13 m^2/g , respectively. The Ag QDs/BiOBr-1 displayed the highest BET surface area but the Ag QDs/BiOBr-0.5 sample exhibited the best photocatalytic activity. Therefore, the BET surface area may be not the dominated factor to determine the photocatalytic activity

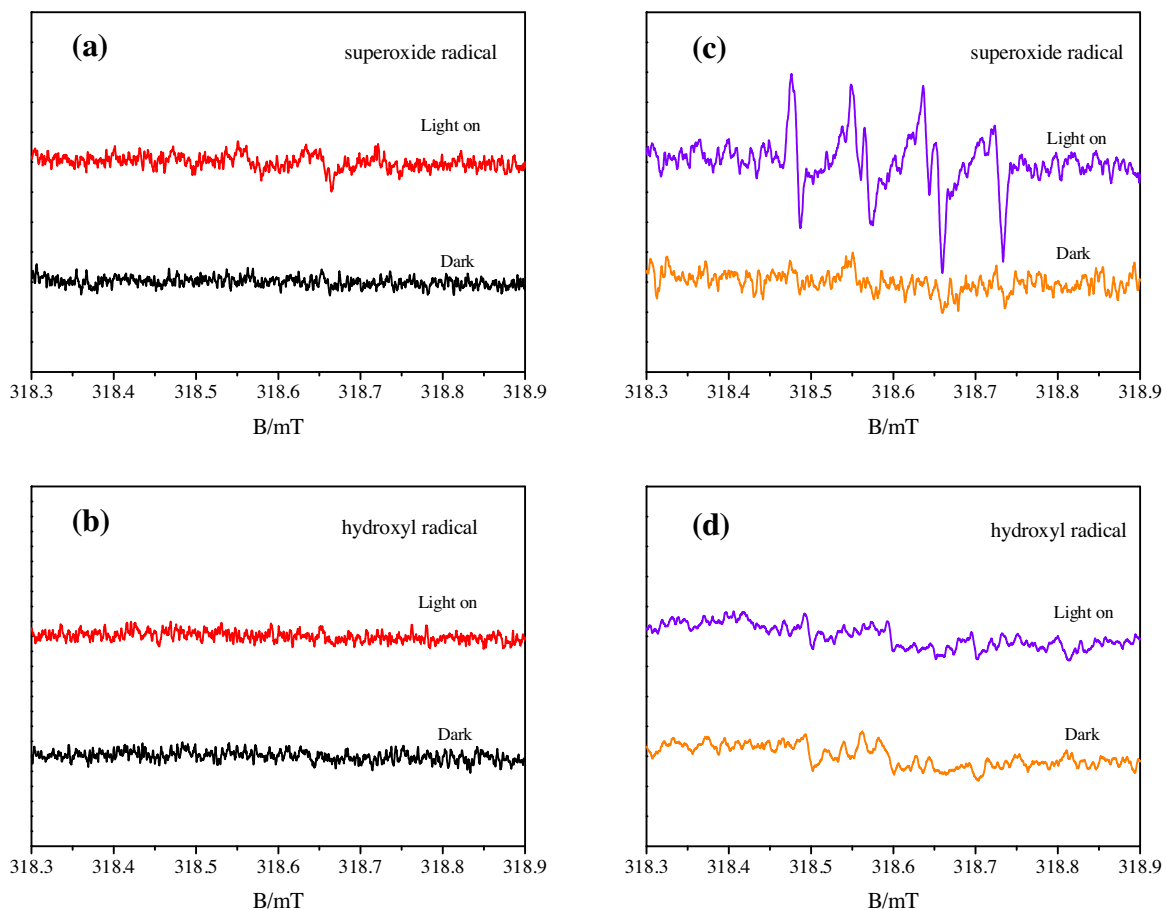


Fig. 12. DMPO spin-trapping ESR spectra of (a, b) BiOBr and (c, d) Ag QDs/BiOBr-0.5 in (a, c) methanol dispersion for DMPO-O_2^- and (b, d) aqueous dispersion (for DMPO-OH^\bullet) in dark or under visible light irradiation.

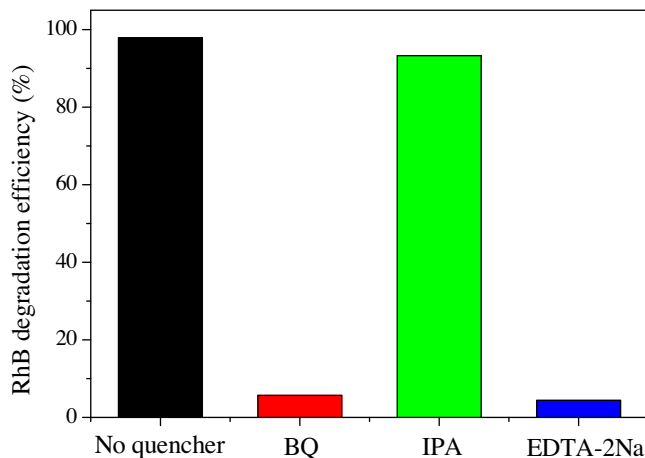


Fig. 13. Comparison of photocatalytic activities of Ag QDs/BiOBr-0.5 materials for the degradation of RhB with or without adding BQ, IPA and EDTA-2Na under visible light irradiation.

in this system. According to the PL and photoelectrochemistry analysis, it can be found that the modification of Ag QDs could improve the separation efficiency of photogenerated charge carriers. As a result, more energetic hot electrons can be obtained and thus more O_2^- can be achieved on the surface of Ag QDs. Since the O_2^- generated on the Ag QDs could degrade the pollutants rapidly, meaning that the Ag QDs could act as photocatalytic reaction centers. Therefore, it was reasonable to suggest that the generated more reactive

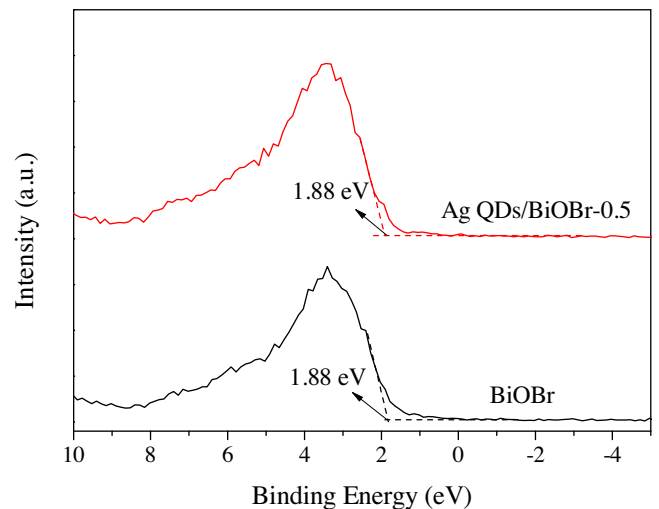


Fig. 14. Valence-band XPS spectra of the BiOBr and Ag QDs/BiOBr-0.5 materials.

O_2^- radical and holes contributed to the high efficient photocatalytic performance of Ag QDs/BiOBr .

Based on the above experimental results, the photocatalytic mechanism diagram of Ag QDs/BiOBr materials was presented in Fig. 15. Under the irradiation of visible light, the electrons in the VB of BiOBr can be excited to the CB and form photo-generated electron-hole pairs. The electrons in the CB could reduce the O_2 to form O_2^- via the one-electron transfer. However, the photo-

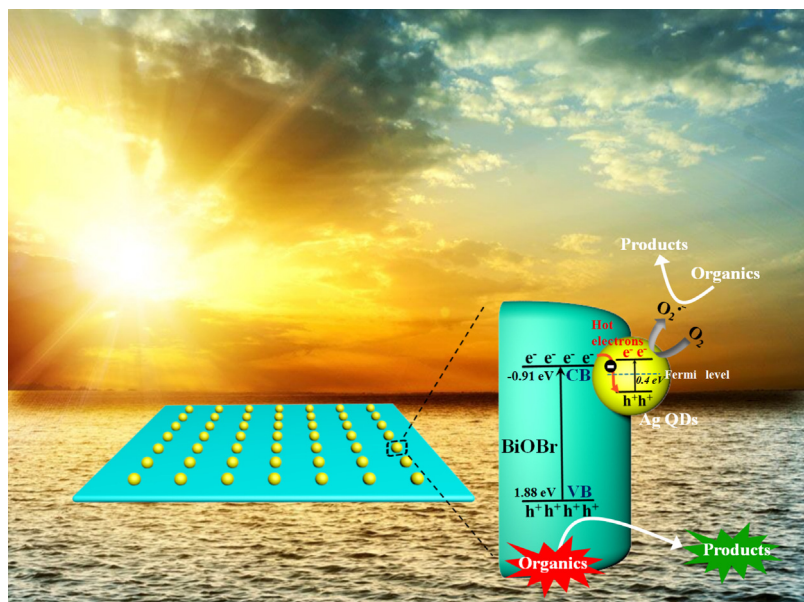


Fig. 15. Schematic diagram illustrating the separation and transfer of photogenerated charges of Ag QDs modified BiOBr materials under visible light irradiation and the possible reaction mechanism.

generated electrons and holes would quickly recombine, thus only bits of $O_2^{\bullet-}$ can be formed and participated in the photocatalysis process. After the Ag QDs was modified on the BiOBr materials, the electron-hole pairs in the Ag QDs can be formed due to the surface plasmon resonance effect. The electrons from the BiOBr would flow into Ag QDs through the Schottky barrier and combined with the holes generated in the Ag QDs. The energetic photogenerated hot electrons in the excited state Ag QDs could active the O_2 via one-electron reduction. The generated $O_2^{\bullet-}$ and the holes on the VB of BiOBr would play important role in the photocatalysis process and endowed the dramatic photocatalytic activity of Ag QDs/BiOBr.

4. Conclusions

The novel Ag QDs modified BiOBr ultrathin nanosheets have been synthesized. The Ag QDs was dispersed on the surface of BiOBr uniformly with the diameter less than 5 nm. The Ag QDs/BiOBr materials displayed vastly superior photocatalytic activity for the degradation of CIP, TC and RhB than pure BiOBr. The Ag QDs could act as adsorption centers, charge separation centers and photocatalytic reaction centers, contributed to the enhanced photocatalytic activity. The main active species were determined to be holes and $O_2^{\bullet-}$ under visible light irradiation and the Ag QDs modification could improve the molecular oxygen activation ability.

Conflict of interest

The authors declare no competing financial interest.

Acknowledgements

This work was financially supported by the National Natural Science Foundation of China (No. 21476098, 21471069 and 21576123), and the science and technology support program of Zhenjiang (SH2014018).

Appendix A. Supplementary data

Supplementary data associated with this article can be found, in the online version, at <http://dx.doi.org/10.1016/j.apcatb.2016.01.062>.

References

- [1] A. Kubacka, M. Fernandez-Garcia, G. Colon, Chem. Rev. 112 (2012) 1555–1614.
- [2] A. Kudo, Y. Miseki, Chem. Soc. Rev. 38 (2009) 253–278.
- [3] J. Di, J.X. Xia, Y.P. Ge, H.P. Li, H.Y. Ji, H. Xu, Q. Zhang, H.M. Li, M.N. Li, Appl. Catal. B 168–169 (2015) 51–61.
- [4] J. Di, J.X. Xia, M.X. Ji, H.P. Li, H. Xu, H.M. Li, R. Chen, Nanoscale 7 (2015) 11433–11443.
- [5] J.S. Zhang, M.W. Zhang, C. Yang, X.C. Wang, Adv. Mater. 26 (2014) 4121–4126.
- [6] H. Li, J. Shang, Z.H. Ai, L.Z. Zhang, J. Am. Chem. Soc. 137 (2015) 6393–6399.
- [7] L. Liang, F.C. Lei, S. Gao, Y.F. Sun, X.C. Jiao, J. Wu, S. Qamar, Y. Xie, Angew. Chem. Int. Ed. 54 (2015) 13971–13974.
- [8] Q.J. Xiang, B. Cheng, J.G. Yu, Angew. Chem. Int. Ed. 54 (2015) 11350–11366.
- [9] H. Liu, W.R. Cao, Y. Su, Y. Wang, X.H. Wang, Appl. Catal. B 111–112 (2012) 271–279.
- [10] K. Awazu, M. Fujimaki, C. Rockstuhl, J. Tominaga, H. Murakami, Y. Ohki, N. Yoshida, T. Watanabe, J. Am. Chem. Soc. 130 (2008) 1676–1680.
- [11] S. Linic, P. Christopher, D.B. Ingram, Nat. Mater. 10 (2011) 911–921.
- [12] F. Dong, T. Xiong, Y.J. Sun, Z.W. Zhao, Y. Zhou, X. Feng, Z.B. Wu, Chem. Commun. 50 (2014) 10386–10389.
- [13] M.J. Kale, T. Avanesian, P. Christopher, ACS Catal. 4 (2014) 116–128.
- [14] D. Yang, Y.Y. Sun, Z.W. Tong, Y. Tian, Y.B. Li, Z.Y. Jiang, J. Phys. Chem. C 119 (2015) 5827–5835.
- [15] X.C. Ma, Y. Dai, L. Yu, Z.Z. Lou, B.B. Huang, M.H. Whangbo, J. Phys. Chem. C 118 (2014) 12133–12140.
- [16] J.T. Li, S.K. Cushing, J. Bright, F.K. Meng, T.R. Senty, P. Zheng, A.D. Bristow, N.Q. Wu, ACS Catal. 3 (2013) 47–51.
- [17] H. Li, L.Z. Zhang, Nanoscale 6 (2014) 7805–7810.
- [18] S. Bai, X.Y. Li, Q. Kong, R. Long, C.M. Wang, J. Jiang, Y.J. Xiong, Adv. Mater. 27 (2015) 3444–3452.
- [19] X.J. Bai, R.L. Zong, C.X. Li, D. Liu, Y.F. Liu, Y.F. Zhu, Appl. Catal. B 147 (2014) 82–91.
- [20] Z.J. Zhang, W.Z. Wang, E.P. Gao, S.M. Sun, L. Zhang, J. Phys. Chem. C 116 (2012) 25898–25903.
- [21] L.Q. Ye, J.Y. Liu, C.Q. Gong, L.H. Tian, T.Y. Peng, L. Zan, ACS Catal. 2 (2012) 1677–1683.
- [22] H.F. Cheng, B.B. Huang, P. Wang, Z.Y. Wang, Z.Z. Lou, J.P. Wang, X.Y. Qin, X.Y. Zhang, Y. Dai, Chem. Commun. 47 (2011) 7054–7056.
- [23] J. Li, Y. Yu, L.Z. Zhang, Nanoscale 6 (2014) 8473–8488.
- [24] M.L. Guan, C. Xiao, J. Zhang, S.J. Fan, R. An, Q.M. Cheng, J.F. Xie, M. Zhou, B.J. Ye, Y. Xie, J. Am. Chem. Soc. 135 (2013) 10411–10417.
- [25] Y.H. Wu, B. Yuan, M.R. Li, W.H. Zhang, Y. Liu, C. Li, Chem. Sci. 6 (2015) 1873–1878.

[26] H.P. Li, J.Y. Liu, X.F. Liang, W.G. Hou, X.T. Tao, *J. Mater. Chem. A* 2 (2014) 8926–8932.

[27] J. Di, J.X. Xia, Y.P. Ge, L. Xu, H. Xu, M.Q. He, Q. Zhang, H.M. Li, *J. Mater. Chem. A* 2 (2014) 15864–15874.

[28] J. Di, J.X. Xia, S. Yin, H. Xu, L. Xu, Y.G. Xu, M.Q. He, H.M. Li, *J. Mater. Chem. A* 2 (2014) 5340–5351.

[29] L.Q. Ye, J.N. Chen, L.H. Tian, J.Y. Liu, T.Y. Peng, K.J. Deng, L. Zan, *Appl. Catal. B* 130–131 (2013) 1–7.

[30] J. Jiang, K. Zhao, X.Y. Xiao, L.Z. Zhang, *J. Am. Chem. Soc.* 134 (2012) 4473–4476.

[31] L.L. Li, L.H. Ai, C.H. Zhang, J. Jiang, *Nanoscale* 6 (2014) 4627–4634.

[32] K. Li, H.B. Zhang, Y.P. Tang, D.W. Ying, Y.L. Xu, Y.L. Wang, J.P. Jia, *Appl. Catal. B* 164 (2015) 82–91.

[33] J. Di, J.X. Xia, S. Yin, H. Xu, M.Q. He, H.M. Li, L. Xu, Y.P. Jiang, *RSC Adv.* 3 (2013) 19624–19631.

[34] H.J. Zhang, Y.X. Yang, Z. Zhou, Y.P. Zhao, L. Liu, *J. Phys. Chem. C* 118 (2014) 14662–14669.

[35] D. Zhang, J. Li, Q.G. Wang, Q.S. Wu, *J. Mater. Chem. A* 1 (2013) 8622–8629.

[36] G.H. Jiang, X.H. Wang, Z. Wei, X. Li, X.G. Xi, R.B. Hu, B.L. Tang, R.J. Wang, S. Wang, T. Wang, W.X. Chen, *J. Mater. Chem. A* 1 (2013) 2406–2410.

[37] J. Di, J.X. Xia, M.X. Ji, S. Yin, H.P. Li, H. Xu, Q. Zhang, H.M. Li, *J. Mater. Chem. A* 3 (2015) 15108–15118.

[38] J. Shang, W.C. Hao, X.J. Lv, T.M. Wang, X.L. Wang, Y. Du, S.X. Dou, T.F. Xie, D.J. Wang, J.O. Wang, *ACS Catal.* 4 (2014) 954–961.

[39] J. Di, J.X. Xia, Y.P. Ge, L. Xu, H. Xu, J. Chen, M.Q. He, H.M. Li, *Dalton Trans.* 43 (2014) 15429–15438.

[40] J. Di, J.X. Xia, M.X. Ji, B. Wang, S. Yin, Q. Zhang, Z.G. Chen, H.M. Li, *Appl. Catal. B* 183 (2016) 254–262.

[41] L. Zhang, W.Z. Wang, S.M. Sun, Y.Y. Sun, E.P. Gao, Z.J. Zhang, *Appl. Catal. B* 148–149 (2014) 164–169.

[42] J.X. Xia, J. Di, H.T. Li, H. Xu, H.M. Li, S.J. Guo, *Appl. Catal. B* 181 (2016) 260–269.

[43] W.Q. Cui, W.J. An, L. Liu, J.S. Hu, Y.H. Liang, *J. Hazard. Mater.* 280 (2014) 417–427.

[44] H.W. Huang, X. Han, X.W. Li, S.C. Wang, P.K. Chu, Y.H. Zhang, *ACS Appl. Mater. Interfaces* 7 (2015) 482–492.

[45] X.X. Wei, C.M. Chen, S.Q. Guo, F. Guo, X.M. Li, X.X. Wang, H.T. Cui, L.F. Zhao, W. Li, *J. Mater. Chem. A* 2 (2014) 4667–4675.

[46] F.T. Li, Q. Wang, J.R. Ran, Y.J. Hao, X.J. Wang, D.S. Zhao, S.Z. Qiao, *Nanoscale* 7 (2015) 1116–1125.

[47] Y.F. Sun, Z.H. Sun, S. Gao, H. Cheng, Q.H. Liu, J.Y. Piao, T. Yao, C.Z. Wu, S.L. Hu, S.Q. Wei, Y. Xie, *Nat. Commun.* 3 (2012) 1057.

[48] S.J. Guo, X. Zhang, W.L. Zhu, K. He, D. Su, A. Mendoza-Garcia, S.F. Ho, G. Lu, S.H. Sun, *J. Am. Chem. Soc.* 136 (2014) 15026–15033.

[49] Y.J. Chen, G.H. Tian, Y.H. Shi, Y.T. Xiao, H.G. Fu, *Appl. Catal. B* 164 (2015) 40–47.

[50] S.X. Weng, B.B. Chen, L.Y. Xie, Z.Y. Zheng, P. Liu, *J. Mater. Chem. A* 1 (2013) 3068–3075.

[51] J. Di, J.X. Xia, M.X. Ji, B. Wang, X.W. Li, Q. Zhang, Z.G. Chen, H.M. Li, *ACS Sustain. Chem. Eng.* 4 (2016) 136–146.

[52] J.G. Yu, J.X. Low, W. Xiao, P. Zhou, M. Jaroniec, *J. Am. Chem. Soc.* 136 (2014) 8839–8842.

[53] Y.F. Sun, S. Gao, F.C. Lei, Y. Xie, *Chem. Soc. Rev.* 44 (2015) 623–636.

[54] H.B. Yin, X.F. Chen, R.J. Hou, H.J. Zhu, S.Q. Li, Y.N. Huo, H.X. Li, *ACS Appl. Mater. Interfaces* 7 (2015) 20076–20082.

[55] Y.L. Li, Y.M. Liu, J.S. Wang, E. Uchaker, Q.F. Zhang, S.B. Sun, Y.X. Huang, J.Y. Li, G.Z. Cao, *J. Mater. Chem. A* 1 (2013) 7949–7956.

[56] J. Chen, M.L. Guan, W.Z. Cai, J.J. Guo, C. Xiao, G.K. Zhang, *Phys. Chem. Chem. Phys.* 16 (2014) 20909–20914.

[57] J. Di, J.X. Xia, M.X. Ji, B. Wang, S. Yin, Q. Zhang, Z.G. Chen, H.M. Li, *ACS Appl. Mater. Interfaces* 7 (2015) 20111–20123.

[58] J. Di, J.X. Xia, S. Yin, H. Xu, L. Xu, Y.G. Xu, M.Q. He, H.M. Li, *RSC Adv.* 4 (2014) 14281–14290.

[59] M. Zhang, X.J. Bai, D. Liu, J. Wang, Y.F. Zhu, *Appl. Catal. B* 164 (2015) 77–81.

[60] G. Zhang, Z.Y. Hu, M. Sun, Y. Liu, L.M. Liu, H.J. Liu, C.P. Huang, J.H. Qu, J.H. Li, *Adv. Funct. Mater.* 25 (2015) 3726–3734.

[61] Y.Y. Zhu, Y.F. Liu, Y.H. Lv, Q. Ling, D. Liu, Y.F. Zhu, *J. Mater. Chem. A* 2 (2014) 13041–13048.

[62] J. Di, J.X. Xia, M.X. Ji, L. Xu, S. Yin, Q. Zhang, Z.G. Chen, H.M. Li, *Carbon* 98 (2016) 613–623.

[63] Y.X. Yang, Y.N. Guo, F.Y. Liu, X. Yuan, Y.H. Guo, S.Q. Zhang, W. Guo, M.X. Huo, *Appl. Catal. B* 142–143 (2013) 828–837.

[64] J.T. Li, S.K. Cushing, J. Bright, F.K. Meng, T.R. Senty, P. Zheng, A.D. Bristow, N.Q. Wu, *ACS Catal.* 3 (2012) 47–51.